Energy Storage Materials 77 (2025) 104232

Contents lists available at ScienceDirect

Energy Storage Materials

journal homepage: www.elsevier.com/locate/ensm

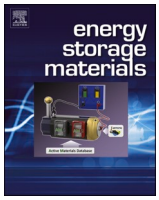

Dendrite-free aluminum metal anode enabled by work function engineering

Shunlong Ju [a], Xiaoyue Zhang [a], Chaoqun Li [a], Yingxue Li [a], Panyu Gao [a], Sihan Yin [c], Tengfei Zhang [c], Guanglin Xia [a], Baozhong Liu [b,*], Xuebin Yu [a,*]

[a] Department of Materials Science, Fudan University, Shanghai 200433, China
[b] College of Chemistry and Chemical Engineering, Henan Polytechnic University, Jiaozuo 454000, China
[c] College of Materials Science and Technology, Nanjing University of Aeronautics and Astronautics, Nanjing 210016, China

ARTICLE INFO

Keywords:
Aluminum-ion battery
Aluminum anode
MXene
Work function
Desolvation

ABSTRACT

The uncontrolled deposition behavior, sluggish reaction kinetics and inefficient utilization of Al derived from unstable anode/electrolyte interface have severely impeded the development of aluminum-ion batteries. Here, we discuss the impact of interfacial electron/ion transfer on the electrochemical performance, and as an illustration, propose the construction of Cu@MXene as anodic current collector through work function engineering to simultaneously achieve homogeneous deposition morphology and rapid plating/stripping rate. The difference in work function between Cu nanoparticles and Ti_3C_2 MXene facilitates charge redistribution in the anode/electrolyte interface and enhances the electron availability, optimizing the interfacial electron/ion transfer behavior. This, in turn, endows Cu@MXene with elevated catalytic efficiency for desolvation reactions and robust reduction ability for the Al plating process. As a result, Cu@MXene enables a high coulombic efficiency of 99.87 % even at a high current density of 10 mA cm^{-2}, and sustains reversible Al plating/stripping cycles for over 3200 h at a typical current density of 1 mA cm^{-2}. Notably, by coupling graphite cathode and Cu@MXene-Al anode under a limited N/P ratio of 2.2, the full cell exhibits durable lifetime for 2000 cycles with an impressive energy density of 119.6 Wh kg^{-1} (based on the total mass of cathode and anode). This work highlights a fundamental understanding of interfacial interactions in the Al deposition process and offer sustainability motivations in designing highly reversible anodes for high-energy-density aluminum-ion batteries.

1. Introduction

The rapid growth and adoption of electrochemical energy storage in our society calls for developing next-generation batteries that combine high energy density and low cost [1–3]. Benefiting from the crustal abundance and high volumetric capacity (8040 mAh cm^{-3} for Al versus 2046 mAh cm^{-3} for Li) of metallic Al anode, rechargeable aluminum-ion batteries (AIBs) are expected to offer substantial improvements in energy density and affordability, representing important choice for post lithium-ion batteries [4–6]. However, a formidable obstacle in the development of viable AIBs lies in the inadequate Al utilization rate and cycling stability of the Al metal anode [7–9]. This could be attributed to the nonuniform Al deposition and severe cracking pulverization during the Al plating/stripping processes, ultimately leading to a decrease in the energy density and lifespan of AIBs [10–12].

To date, various strategies such as electrode surface modification, the design of anodic current collector, and the synthesis of Al-based alloy have been employed to achieve stable Al anode [13–18]. Among them, the construction of an aluminophilic current collectors is undoubtedly considered as a promising and effective method [19]. It has been shown that the novel current collectors, on the one hand, possess the capability to guide uniform Al deposition, enhancing reversibility and extending cycle life. On the other hand, they are anticipated to boost Al utilization, minimize the quantity of anode material, and elevate cell-level energy density [20–22]. Despite significant improvements in the reversibility and stability of anodic current collectors in previous research, their kinetic properties remain unsatisfactory. Low coulombic efficiency (CE), large overpotential, and dendrite growth still exist when the battery is operated with a high current density and large areal capacity.

A typical Al deposition reaction in $AlCl_3$/[EMIm]Cl ionic liquid electrolyte includes two steps, i.e. the desolvation of chloroaluminate ions and the adsorption of Al^{3+} ions (Scheme 1). Al^{3+} ions are first released from $Al_2Cl_7^-$ anions, and then adsorbed on the current collectors to obtain the deposition layer [23]. During the desolvation process, the

* Corresponding authors.
E-mail addresses: bzliu@hpu.edu.cn (B. Liu), yuxuebin@fudan.edu.cn (X. Yu).

https://doi.org/10.1016/j.ensm.2025.104232
Received 21 January 2025; Received in revised form 9 March 2025; Accepted 3 April 2025
Available online 3 April 2025
2405-8297/© 2025 Published by Elsevier B.V.

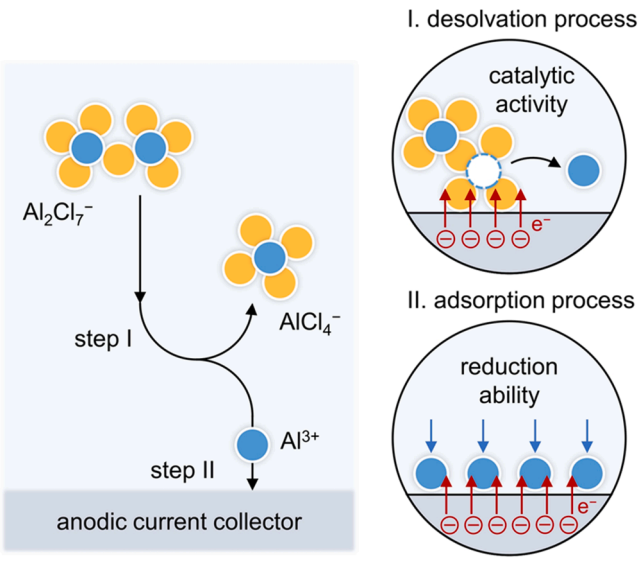

Scheme 1. Schematic illustration of the Al plating process on anodic current collector in $AlCl_3$/[EMIm]Cl ionic liquid electrolyte.

interfacial electron transfer from the current collector to the chloroaluminate ions causes the destabilization of the Al—Cl bonds, thereby facilitating the dissociation of Al^{3+}, which serves as a catalytic effect [24]. In the subsequent adsorption process, the abundant and uniform interfacial electron flux from the current collector to the Al^{3+} ions is responsible for the reduction of Al^{3+} to smooth Al plating layer [25]. Therefore, the interfacial electron/ion transfer plays key role in the desolvation rate and adsorption efficiency on the current collectors, exerting considerable influence on the Al plating/stripping behaviors, especially the kinetic properties. Based on the above discussions, an ideal anodic current collector for advanced AIBs should possess the following crucial features: (1) a high catalytic activity for promoting desolvation reactions, and (2) the ability to provide sufficient electrons to the adsorbates to ensure desolvation and reduction performance. Nevertheless, the development of a current collector that meets all these criteria has yet to be realized, and the underlying design principles are still unclear, presenting a notable challenge in this field.

In this work, we introduce work function engineering to design a novel Al current collector that simultaneously fulfill the aforementioned criteria to improve the stability and rate capability. Specifically, Cu nanoparticles (NPs) embedded onto Ti_3C_2 MXene (Cu@MXene) are prepared as a current collector to optimize the Al plating/stripping behaviors, in which the monodispersed Cu NPs serve as catalytic and aluminophilic sites, while MXene acts as an electron donor. The difference in work function (W_f) drives electrons to migrate from MXene to Cu. This enhanced electron availability in Cu NPs elevates its catalytic activity and reduction capability, thereby facilitating desolvation reactions and ensuring homogeneous Al^{3+} flux distribution. Benefiting from these merits, we achieve a uniform and compact Al deposition morphology, as well as remarkable stability and rate performance. The Cu@MXene current collector demonstrates a high CE of 99.87 % for Al plating/stripping processes even at a high current density of 10 mA cm^{-2}. Meanwhile, the symmetric cell with Cu@MXene-Al anode could stable cycle for over 2000 h at 5 mA cm^{-2} and 5 mAh cm^{-2}, delivering an impressive cumulative plated capacity of 5 Ah cm^{-2}. Furthermore, the high Al utilization rate and superior reversibility of the Cu@MXene-Al anode enable Al full cells to exhibit stable cycling performance and high energy density under a low N/P ratio. This work provides a fresh insight into the design of current collectors with rapid kinetic properties and prolonged lifespan, and presents guidance for improving the anode/electrolyte interface in AIBs.

2. Results and discussion

The concept of utilizing Cu@MXene as an anodic collector in AIBs is first investigated theoretically through density functional theory (DFT) calculations. Due to their lowest surface energies of 0.77 J m^{-2} and 1.33 J m^{-2}, respectively, the most stable Al(111) and Cu(111) slabs are selected for simulating metallic Al and Cu in all calculations (Fig. S1a, b). And Cu@MXene is represented by a model of Cu cluster loaded on the surface of Ti_3C_2 MXene (Fig. S1c). In this scenario, the electrostatic potential across the material-vacuum interface is calculated to determine the theoretical W_f. As depicted in Fig. S2, the theoretical W_f of Cu (111) is 4.82 eV, exceeding that of MXene (4.44 eV). This discrepancy in W_f would induce a contact potential within the Cu@MXene composite, driving electrons to migrate from MXene to Cu (Fig. 1a) [26]. This phenomenon is further substantiated by the observation that approximately 0.3|e| accumulates on each Cu atom in Cu@MXene (Fig. 1b). Compared to Cu(111), Cu@MXene exhibits increased electron availability and donates more electrons to the adsorbed ions (e.g. $Al_2Cl_7^-$, $AlCl_4^-$ and Al^{3+} in Fig. 1c), potentially enhancing its catalytic activity and reduction capability [27].

The desolvation processes of chloroaluminate ions on Al(111), Cu (111) and Cu@MXene, which involves the stepwise decomposition of $Al_2Cl_7^-$ to form $AlCl_4^-$, $AlCl_2^+$, $AlCl^{2+}$ intermediates and the final product Al^{3+}, are simulated to investigate their kinetic properties. Based on the optimized adsorption configurations of chloroaluminate ions on these substrates (Fig. S3), the corresponding Gibbs free energy profiles in Fig. 1d show the endothermic nature of the desolvation reactions. Among them, the conversion from $AlCl_4^-$ to $AlCl_2^+$ demonstrates the largest Gibbs free energy change (ΔG), thereby being identified as the rate-limiting step. A decrease in ΔG, from 3.58 eV on Al(111) to 3.00 eV on Cu(111), suggests the catalytic effect of metallic Cu in facilitating the dissociation reactions. Notably, the introduction of MXene results in a further decrease of ΔG to 2.18 eV, emphasizing the boosted desolvation kinetics and enhanced catalytic activity of Cu@MXene. This improvement could be attributed to the significant charge redistribution between Cu@MXene and chloroaluminate ions, which effectively destabilizes Al—Cl bonds as evidenced by the increased bond lengths (Fig. S4). Furthermore, Cu@MXene, with its higher binding energies for $Al_2Cl_7^-$, $AlCl_4^-$ and Al^{3+} compared to Al(111) and Cu(111), promotes the adsorption of chloroaluminate ions and the reduction of Al^{3+} to Al atoms on its surface (Fig. 1e) [28]. This observation corroborates that the charge accumulation on Cu@MXene contributes to its high aluminophilicity and robust reduction capability. In addition, the diffusion barrier of a single Al atom is as low as 57 meV on Cu(111) and 150 meV on MXene (Fig. S5). This unhindered diffusion pattern is responsible for the uniform distribution of Al atoms without local aggregation, which is conducive to homogeneous Al deposition. On the basis of above calculations, Cu@MXene is expected to be a promising anodic current collector with strong aluminophilicity and rapid plating/stripping kinetics, thus achieving long-term durability, superior rate performance and high Al utilization rate.

Under the guidance of theoretical analysis, Cu NPs are homogeneously embedded on the surface of MXene sheets using an electrostatic self-assembly method to synthesize Cu@MXene [29]. The few-layer MXene is first prepared by etching the MAX phase followed by ultrasonication (Fig. S6). Subsequently, positively charged Cu^{2+} ions are introduced into the MXene dispersion, and after annealing, uniform anchoring of Cu NPs on the MXene sheets is achieved. The Cu content in Cu@MXene is determined to be ~7.4 wt.% by inductively coupled plasma optical emission spectroscopy (ICP-OES). In the X-ray diffraction (XRD) patterns in Fig. 1f, all diffraction peaks could be indexed to MXene phase and metallic Cu, clearly suggesting the formation of high-purity, crystalline Cu NPs inside Cu@MXene [30]. The X-ray photoelectron spectroscopy (XPS) of Cu@MXene reveals the presence of an energy band at around 929.3 eV, which is associated with the characteristic peak of Cu 2p, and the high-resolution Cu 2p spectrum could

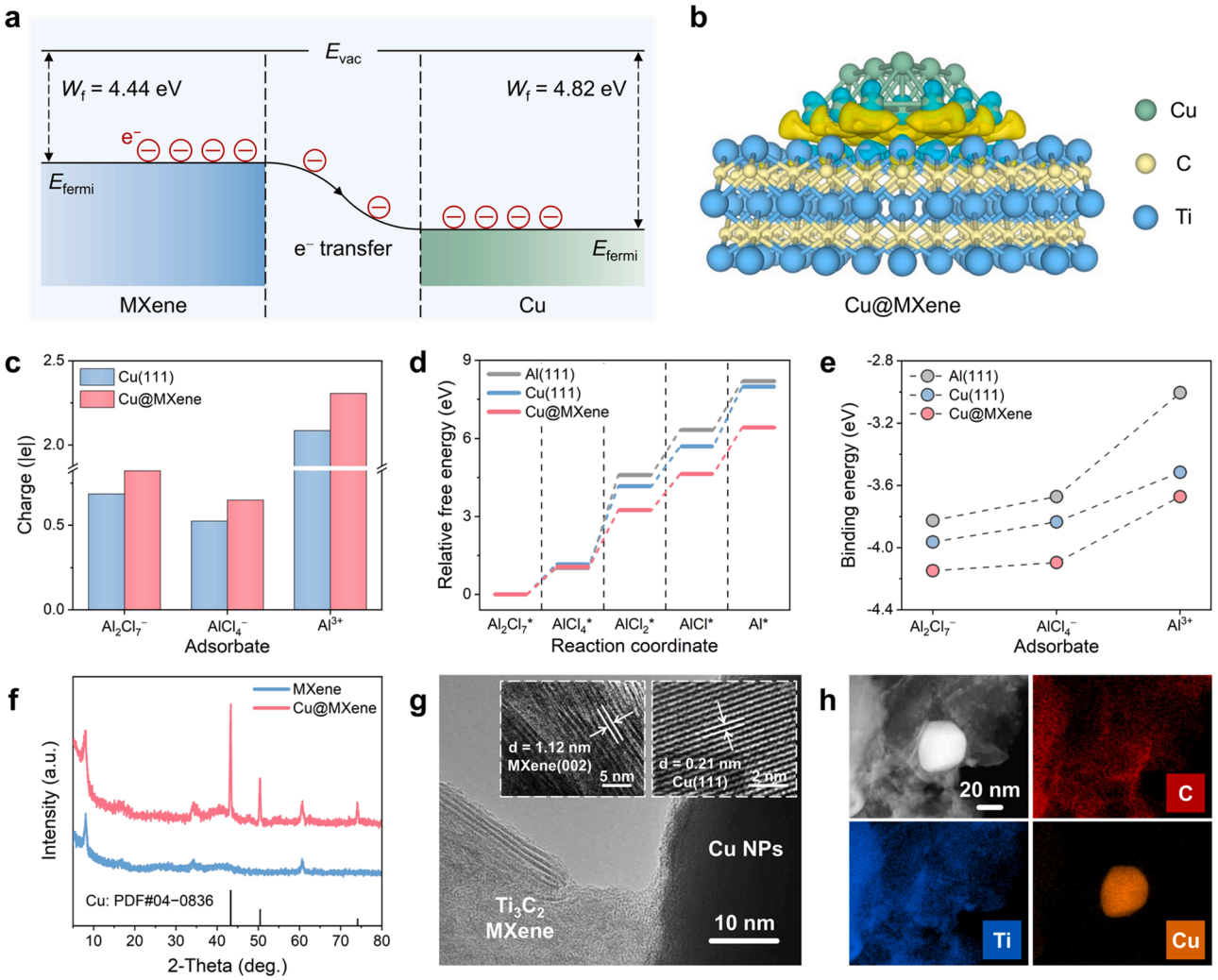

Fig. 1. Material design and characterizations. a) Energy-band plots of MXene and Cu (E_{vac}: vacuum level; E_{fermi}: Fermi level; W_f: work function). b) Charge density difference plots of Cu@MXene. Areas of charge accumulation are shown in yellow while depletion are shown in blue. The isosurface value is 0.005 e Å^{-3}. c) The amount of charge transferred from Cu(111) and Cu@MXene to Al^{3+}, $AlCl_4^-$ and $Al_2Cl_7^-$. d) Relative free energy profiles for the desolvation process of $Al_2Cl_7^-$ on Al (111), Cu(111), and Cu@MXene. Energies were normalized against the energy of the $Al_2Cl_7^-$ ion on each substrate. e) Binding energies of Al^{3+}, $AlCl_4^-$ and $Al_2Cl_7^-$ on Al (111), Cu(111), and Cu@MXene. f) XRD patterns of MXene and Cu@MXene. g) HRTEM images of Cu@MXene. h) HADDF-STEM image and corresponding EDS element mapping images of Cu@MXene.

be resolved into two components, i.e. the prominent Cu^0 and the minor Cu^{2+} (Fig. S7). Moreover, Cu LMM Auger spectrum is recorded to distinguish Cu^+ from Cu^0. As depicted in Fig. S8, the characteristic peak corresponding to Cu^+ is not observed, corroborating the absence of Cu^+ in the sample. The kinetic energy locating at 918.6 eV indicates the dominant Cu^0 in Cu@MXene, providing further evidence to the existence of zero-valent copper [31]. Scanning electron microscopy (SEM) and transmission electron microscopy (TEM) are then employed to investigated the morphology of Cu@MXene. Flexible MXene sheets offer robust structural support to the uniformly anchored Cu NPs, whose particle sizes range from 10 to 20 nm (Fig. S9). High-resolution TEM (HRTEM) images in Fig. 1g illustrate lattice fringes of 1.12 nm and 0.21 nm, corresponding to the interlayer spacing of MXene(002) and Cu (111), respectively. As shown in Fig. 1h, high-angle annular dark-field scanning TEM (HAADF-STEM) imaging accompanied by energy-dispersive spectroscopy (EDS) elemental mapping analysis directly recognizes Cu NPs on the MXene sheets surface. Additionally, the Brunauer–Emmett–Teller (BET) specific surface area of Cu@MXene (24.2 $m^2\ g^{-1}$) exceeds that of MXene (5.8 $m^2\ g^{-1}$). This feature endows Cu@MXene with more active sites and an extensive route for the mass transfer process (Fig. S10). All the aforementioned results collectively demonstrate the successful construction of the Cu@MXene matrix.

Ultraviolet photoelectron spectroscopy (UPS) is utilized to verify the local electronic environment in the actual samples. As shown in Fig. S11, W_f of Cu and MXene are determined to be 4.48 eV and 3.26 eV, respectively. The discrepancy between theoretical and experimental values might arise from the idealized surface model in simulations. Despite this, both DFT calculations and UPS results confirm that Cu exhibits a higher W_f than MXene, corroborating the design of Cu@MXene for charge-transfer-mediated functionalities. Ex situ XRD in Fig. S12 decipher the electrochemical reactions occurring on Cu foil, MXene and Cu@MXene during the Al plating/stripping processes. Notably, only diffraction peaks corresponding to metallic Al could be newly detected after Al deposition, and these peak intensities gradually increase over time. This indicates that Al nucleates and grows on these substrates without any additional alloying or chemical reactions. In order to evaluate the desolvation kinetics, electrochemical impedance spectroscopy (EIS) analyses are performed on asymmetric cells by coupling Al foil with Cu, MXene or Cu@MXene (Fig. S13). The charge-transfer resistances of various asymmetric cells at temperatures ranging from 293 K to 333 K are then used to calculate the apparent activation energy (E_a) following the Arrhenius equation. As illustrated in

the Nyquist diagrams in Fig. 2a, Cu@MXene delivers smaller E_a (18.1 kJ mol^{-1}) than Cu (32.4 kJ mol^{-1}) and MXene (39.1 kJ mol^{-1}). The observed discrepancy demonstrates the rapid Al plating/stripping rate on Cu@MXene and its superior catalytic effect towards desolvation reactions, aligning well with the findings obtained from DFT calculations. Fig. 2b depicts the voltage curves for the initial Al plating process at a current density of 1 mA cm^{-2}, where the nucleation overpotentials on Cu foil, MXene, and Cu@MXene are 106.3, 91.0, and 42.3 mV, respectively. Moreover, Cu@MXene exhibits the lowest nucleation overpotential across various current densities, indicating its exceptional aluminophilicity and significant advancements in lowering the Al nucleation barrier as well as facilitating uniform nucleation (Figs. 2c and S14). Therefore, work function engineering endows Cu@MXene with enhanced catalytic activity and reduction capability, substantially improving the Al plating/stripping behavior.

The rate performance of asymmetric Cu@MXene cell is illustrated in Fig. 2d, revealing voltage hysteresis of 38.9, 60.1, 99.8, 147.4, 209.2, and 255.4 mV at current densities of 1, 2, 4, 6, 8, and 10 mA cm^{-2}, respectively. Upon reducing the current density from 10 to 1 mA cm^{-2}, the overpotential returns to its initial level. Additionally, the corresponding average CE is determined to be 99.71 %, confirming the rapid Al plating/stripping kinetics and remarkable reversibility of Cu@MXene under high current densities (Fig. 2e). In contrast, asymmetric cells using Cu and MXene exhibit larger voltage hysteresis and lower CE, and short-circuit when the current density increases to 6 mA cm^{-2}, preventing their operation at high rate (Fig. S15). The superior reversibility of Cu@MXene is further demonstrated over a broad range of areal capacities (from 1 to 50 mAh cm^{-2}), where the voltage profiles remain consistent and the CEs are all higher than 99.3 % (Fig. 2f). These phenomena emphasize the fact that the optimized interfacial electron/ion transport properties empower Cu@MXene to achieve stable Al plating/stripping under high current densities and high areal capacities. In terms of cycling performance, Cu@MXene displays an extended lifespan exceeding 3200 h and a minimal voltage hysteresis of ~37.5 mV at 1 mA cm^{-2} and 1 mAh cm^{-2}, accompanied by an average CE of 99.95 %. After cycling, the uniform distribution of Cu NPs on MXene is verified by SEM images, implying an excellent structural integrity of Cu@MXene (Fig. S16). This robust architecture provided sufficient active sites and assured a long-term stability. By comparison, both Cu foil and MXene exhibit relatively high and fluctuated voltage hysteresis, and short-circuit within 30 h and 150 h, respectively. Therefore, the aforementioned results highlight the impressive stability and reversibility of the Al plating/stripping process on Cu@MXene, which could be attributed to rapid desolvation reactions and homogenous nucleation, benefiting from the work function engineering.

The evolution of Al deposition morphologies on Cu foil, MXene and

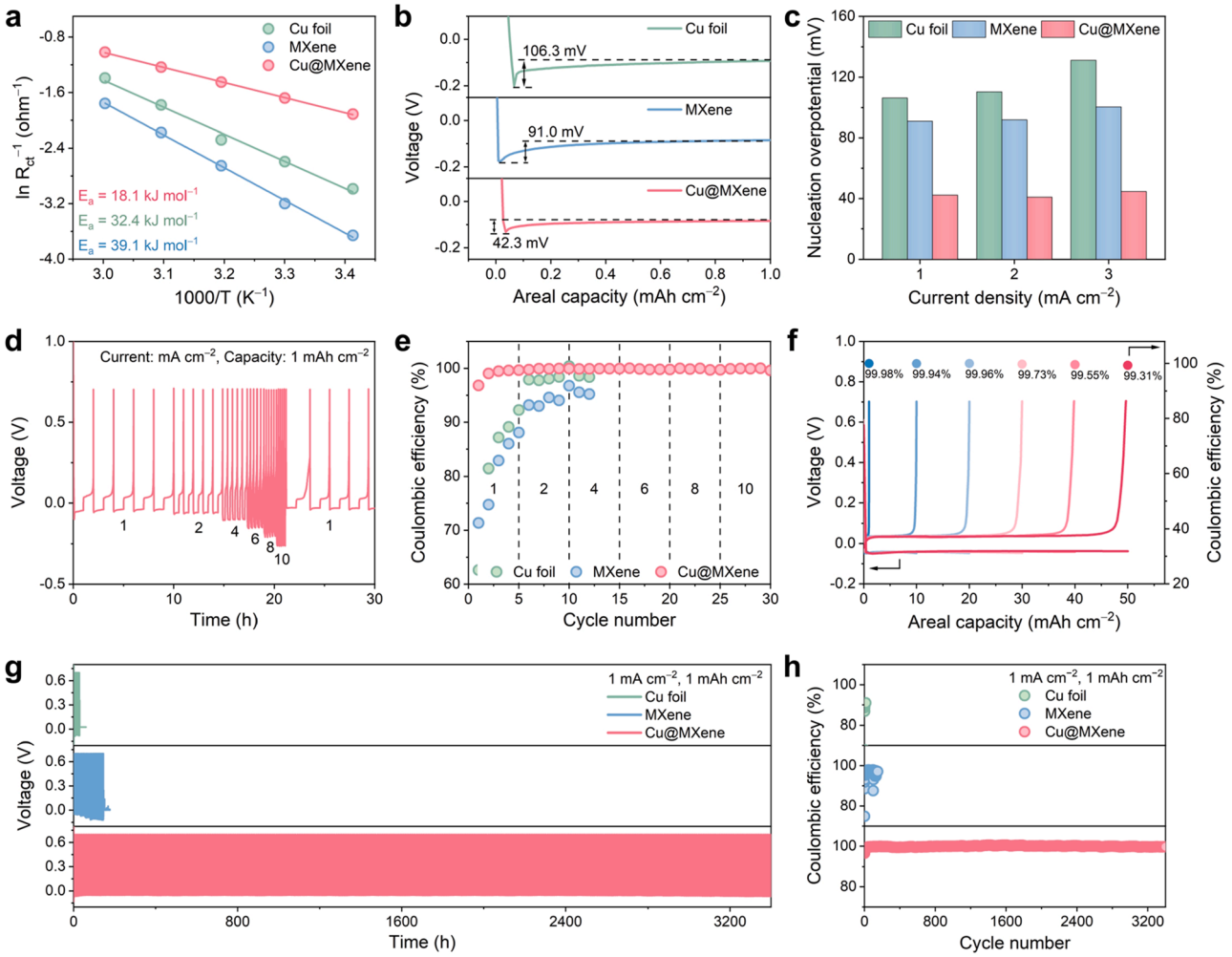

Fig. 2. Al deposition behavior on Cu@MXene. a) Arrhenius images of Cu foil, MXene and Cu@MXene. b) Voltage profiles for the initial Al deposition on Cu foil, MXene and Cu@MXene at 1 mA cm^{-2} and 1 mAh cm^{-2}. c) Nucleation overpotentials of Cu foil, MXene and Cu@MXene at different current densities. d) Rate performance and e) corresponding coulombic efficiency of Cu@MXene at current densities from 1 to 10 mA cm^{-2}. f) Galvanostatic charge/discharge curves of Cu@MXene asymmetry cell under different areal capacities. g) Cycling performance and h) corresponding coulombic efficiency of Cu foil, MXene and Cu@MXene asymmetry cells at 1 mA cm^{-2} and 1 mAh cm^{-2}.

Cu@MXene are investigated by ex situ SEM. As shown in Figs. 3a and S17, Al dendrites emerge on Cu foil with the increase of deposition capacity. On MXene, segmented mossy Al dendrites and protrusion appear accompanied by visible voids and cracks (Figs. 3b and S18). In addition, EDS elemental mappings reveal the inhomogeneous distribution of elemental Al on both Cu foil and MXene. These uncontrolled Al plating behaviors might result in poor reversibility and low Al utilization rate, formidable voltage polarization and, even worse, battery failure. On the contrary, Al uniformly nucleates along the surface of Cu@MXene guided by abundant Cu NPs at a capacity of 1 mAh cm^{-2}. As the areal capacity reaches 3 mAh cm^{-2} and subsequently 5 mAh cm^{-2}, a compact and dendrites-free Al deposition layer gradually evolves and ultimately covers the surface of Cu@MXene (Figs. 3c and S19). From the cross-sectional SEM images in Fig. S20, a much denser deposition structure and reduced volume expansion are observed on Cu@MXene compared to those on Cu foil and MXene electrode, further highlighting its advantage in regulating Al platting behavior. Moreover, the optimized deposition morphology on Cu@MXene is confirmed by the uniform Al distribution in EDS elemental mapping and low surface altitude intercept in laser scanning microscopy (LSM) result (Fig. 3d–f). These phenomena illustrate the effectiveness of Cu@MXene in modulating Al deposition morphology, which is conducive to improve its electrochemical performance.

The electrochemical properties of Al-loaded Cu-Al, MXene-Al and Cu@MXene-Al anodes are investigated in symmetric cells. Compared with Cu-Al and MXene-Al anodes, Cu@MXene-Al delivers a reduced voltage hysteresis of approximately 57.3 mV and a prolonged cycle life exceeding 3000 h (Fig. 3g). Additionally, the Cu@MXene-Al anode exhibits superior rate performance. As depicted in Fig. 3h, when current densities are increased from 1 to 10 mA cm^{-2}, the symmetric cell with Cu@MXene-Al anode displays voltage hysteresis of 33.9, 72.7, 111.1, 175.4, 225.1 and 292.2 mV. In contrast, symmetric cells with Cu-Al or

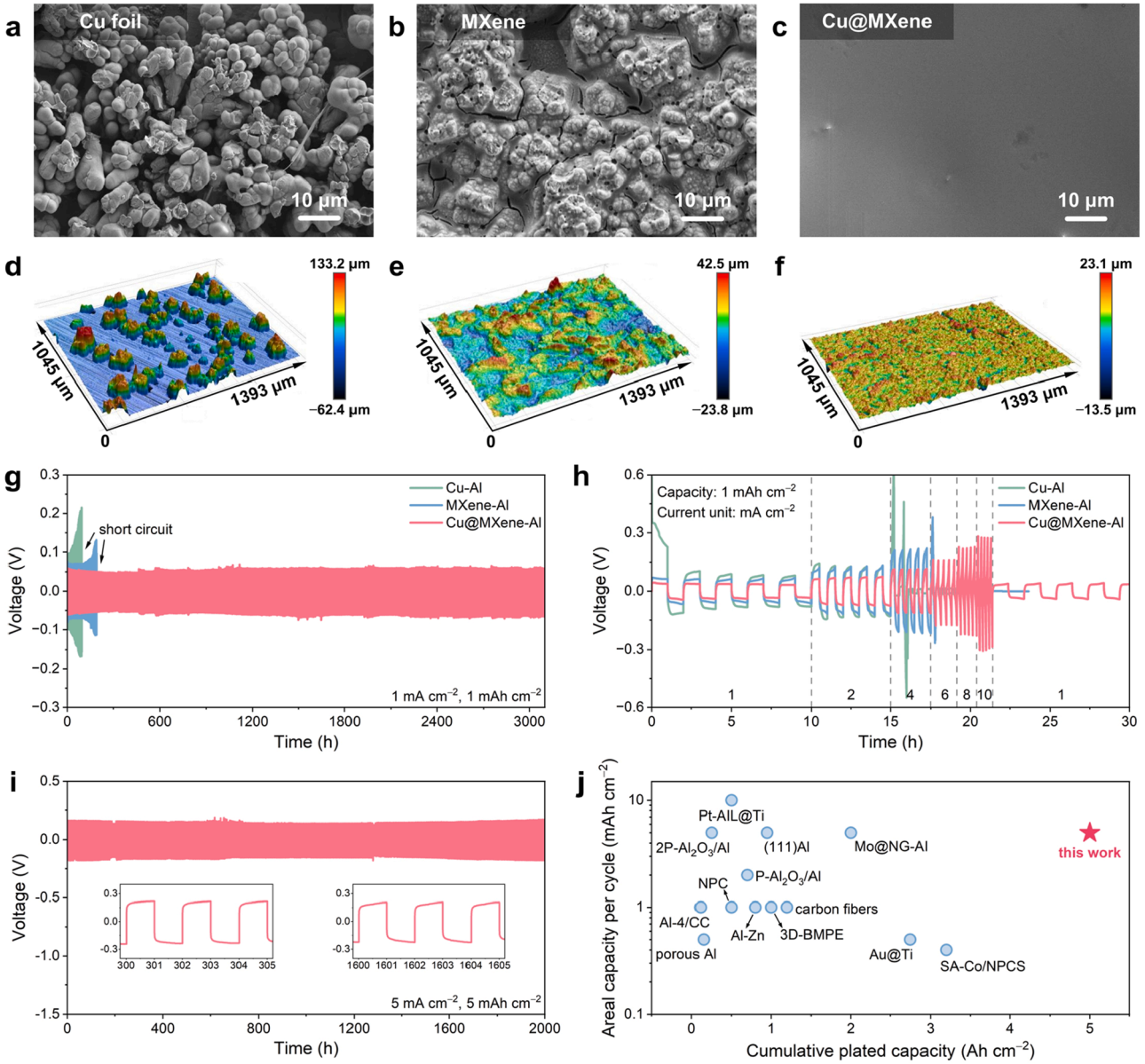

Fig. 3. Morphology and electrochemical performance of Cu@MXene-Al anode. SEM images of a) Cu foil, b) MXene, and c) Cu@MXene with Al deposition capacity of 5 mAh cm^{-2}. LSM image of d) Cu foil, e) MXene, and f) Cu@MXene with Al deposition capacity of 5 mAh cm^{-2}. g) Cycling performance of symmetric cells with Cu-Al, MXene-Al and Cu@MXene-Al at 1 mA cm^{-2} and 1 mAh cm^{-2}. h) Rate performance of symmetric cells with Cu-Al, MXene-Al and Cu@MXene-Al at current densities from 1 to 10 mA cm^{-2}. i) Cycling performance of symmetric cells with Cu@MXene-Al at 5 mA cm^{-2} and 5 mAh cm^{-2}. The insets are the close-up views of the cycling behavior of the symmetric cell at different cycling stages. j) A comparison of Al plating/stripping performance in recent demonstrations with our work.

MXene-Al anodes demonstrate much higher voltage hysteresis and suddenly short-circuit as the current density increases. At a high areal capacity of 10 mAh cm^{-2}, the symmetric cell with Cu@MXene-Al anode shows smooth voltage curves during Al plating/stripping processes and manifest a stable cycling for 1000 h (Fig. S21). The cycling performance of Cu@MXene-Al anode is further evaluated at 5 mA cm^{-2} and 5 mAh cm^{-2}. Even under such stringent condition of high current density and high areal capacity, the Cu@MXene-Al anode still exhibits cycling stability for over 2000 h (Fig. 3i). Notably, this result contributes to a cumulative capacity of 5 Ah cm^{-2}, demonstrating significant advantages compared to the state-of-the-art Al anodes reported in the literatures (Fig. 3j and Table S1). All these measurements highlight the remarkable Al plating/stripping stability and rate capability of Cu@MXene-Al anode, which could be attributed to the integrated merits of superior catalytic activity and enhanced reduction capability derived from work function engineering.

The influence of Cu@MXene on the Al plating process is further explored through finite element simulations using the COMSOL Multiphysics software. As depicted in Fig. S22, the electric field is non-uniformly distributed on the surface of Cu foil and MXene with the local current density concentrated near the nucleation protrusions, which accelerates the Al^{3+} flux to converge toward the nucleus tips and aggravates the uneven deposition, in turn leading to the formation of initial dendrites. These early-stage dendrites further exacerbate the non-uniformity of electric field distribution, eventually resulting in prominent Al dendrites (Fig. 4a–d). On the contrary, uniform distributions of Al^{3+} flux and electric field are found across the interphase between Cu@MXene and electrolyte. In this scenario, the initial Al nuclei homogeneously distribute on the Cu@MXene surface, and then gradually grow and thicken as deposition progresses to form a compact and dendrite-free Al layer (Fig. 4e, f). This improvement could be attributed to the work function engineering that promotes the electron/ion transfer and homogenizes the local current density, thus suppressing the dendrite formation. To summarize, an impressive Cu@MXene substrate is developed via work function engineering strategy, as illustrated in Fig. 4g. By coupling Cu NPs with high W_f and MXene with low W_f, directional migration of ions from MXene to Cu NPs is achieved, which significantly boosts the catalytic activity and reduction capability of Cu.

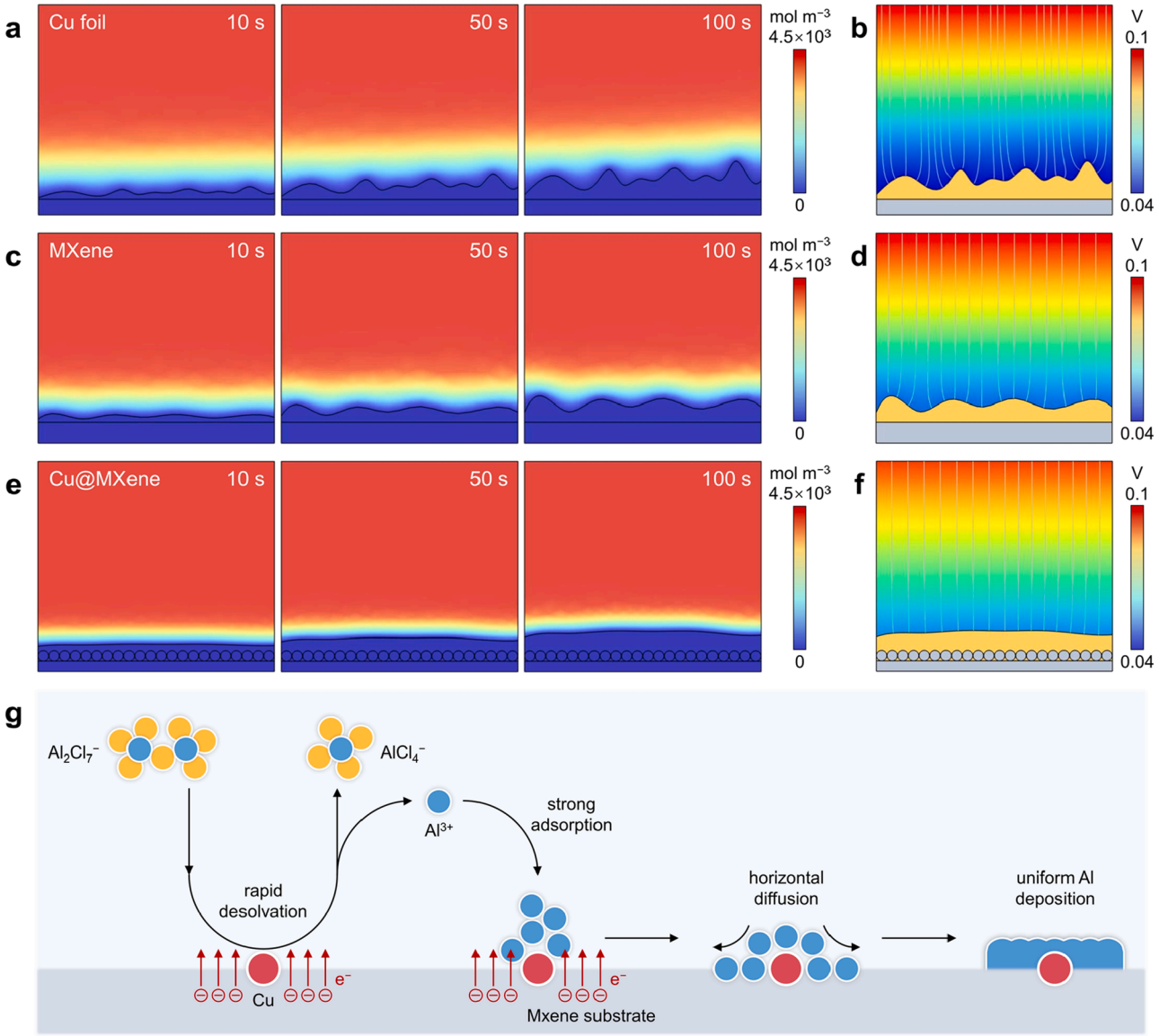

Fig. 4. Finite element simulations and analyses. Al^{3+} concentration and morphological evolution snapshots during Al deposition on a) Cu foil, c) MXene and e) Cu@MXene at selected simulation states. Simulations of the electric field distribution of b) Cu foil, d) MXene and f) Cu@MXene at final state. g) Schematic representation of the optimized Al plating process on Cu@MXene.

This enhancement promotes the desolvation of chloroaluminate ions and facilitates the adsorption and nucleation of Al^{3+}. Combining the rapid diffusion characteristic of Al on both Cu and MXene, a homogeneous deposition morphology is obtained, enabling stable and reversible Al plating/stripping on Cu@MXene, even under high current densities and large areal capacities.

The accelerated Al plating/stripping kinetics, superior reaction reversibility, and extended cycling lifespan of the Cu@MXene-Al anode pave the way to achieve advanced AIBs under a low N/P ratio. The reduction in the N/P ratio implies a decrease in the anode mass, which is poised to significantly lower the battery cost and increase energy density [32,33]. Herein, the feasibility and potential application of the Cu@MXene-Al anode are demonstrated in graphite//Cu@MXene-Al full cell under a controlled N/P ratio of ~2.2. As shown in Fig. S23a, graphite//Cu@MXene-Al exhibits higher specific capacity and smaller voltage polarization in compared with graphite//Al and graphite//MXene-Al full cells. This finding is further supported by the narrower voltage gap between the redox peaks of graphite//Cu@MXene-Al in cyclic voltammetry (CV) curves, manifesting its rapid reaction kinetics and high Al utilization rate (Fig. S23b). Fig. 5a depicts the galvanostatic charge/discharge profiles of graphite//Cu@MXene-Al under current densities varying from 0.1 to 2 A g^{-1}. Noticeably, the plateaus are well maintained, and the specific capacity retains at 95.5 mAh g^{-1} even at 2 A g^{-1}. On the contrary, the specific capacities of both graphite//Al and graphite//MXene-Al full cells decrease drastically as the current density increases (Fig. 5b). In the case of cycling performance, the graphite//Cu@MXene-Al full cell exhibits a reversible specific capacity of 89.5 mAh g^{-1} after 2000 cycles, with a CE of 99.2 % and capacity retention rate of 93.9 % (Fig. 5c). By contrast, fast capacity fading along with low CE are observed in the graphite//Al and graphite//MXene-Al full cells. These results reveal the superior rate capability and long-term cycling stability of the graphite//Cu@MXene-Al full cell under limited N/P ratio, which is attributed to the improved Al plating/stripping behavior on the surface of Cu@MXene-Al anode. Impressively, the energy density (based on the mass of electrode) of the graphite//Cu@MXene-Al full cell is determined as 119.6 Wh kg^{-1} (Table S2). This parameter is among the highest values compared with AIBs using carbonaceous cathode in the literatures (Fig. 5d) [14,19,24,34–42]. Note that most of the previous work utilized impractical full-cell components that incorporated excess Al to prevent its depletion, or suffered from capacity degradation at low N/P ratio (Table S3). Here, advancements in achieving a low N/P ratio and high capacity retention are realized simultaneously through the development of Cu@MXene current collector with optimized interfacial electron/ion transfer via work function engineering, which represents an important step towards the practical AIBs application. Although further efforts are required to construct high-energy-density AIBs with limited N/P ratios, lean electrolytes and large capacities, our research provides a solid foundation for such goals.

3. Conclusions

In this contribution, we presented an innovative Cu@MXene scaffold via work function engineering to tailor the interfacial stability and deposition morphology of Al anode. The optimized interfacial electron/ion transfer modulates the desolvation, nucleation and growth behavior, which promotes the spatially uniform distribution of Al nuclei, favoring a dense deposition layer with low voltage hysteresis. These merits enable Cu@MXene to achieve highly reversible Al plating/stripping for 3200 h with an average CE of 99.95 %. Accordingly, the Cu@MXene-Al anode exhibits stable cycling performances at high current densities and capacities of 5 mA cm^{-2} and 5 mAh cm^{-2}. When coupled with graphite cathode, the graphite//Cu@MXene-Al full cell delivers prolonged lifespan of 2000 cycles, and a superior energy density of 119.6 Wh kg^{-1} under a low N/P ratio of 2.2. Such a work function engineering provides a novel path to solve the utilization and dendrite problems of metallic Al anodes.

CRediT authorship contribution statement

Shunlong Ju: Writing – review & editing, Writing – original draft, Visualization, Investigation, Funding acquisition, Formal analysis, Data

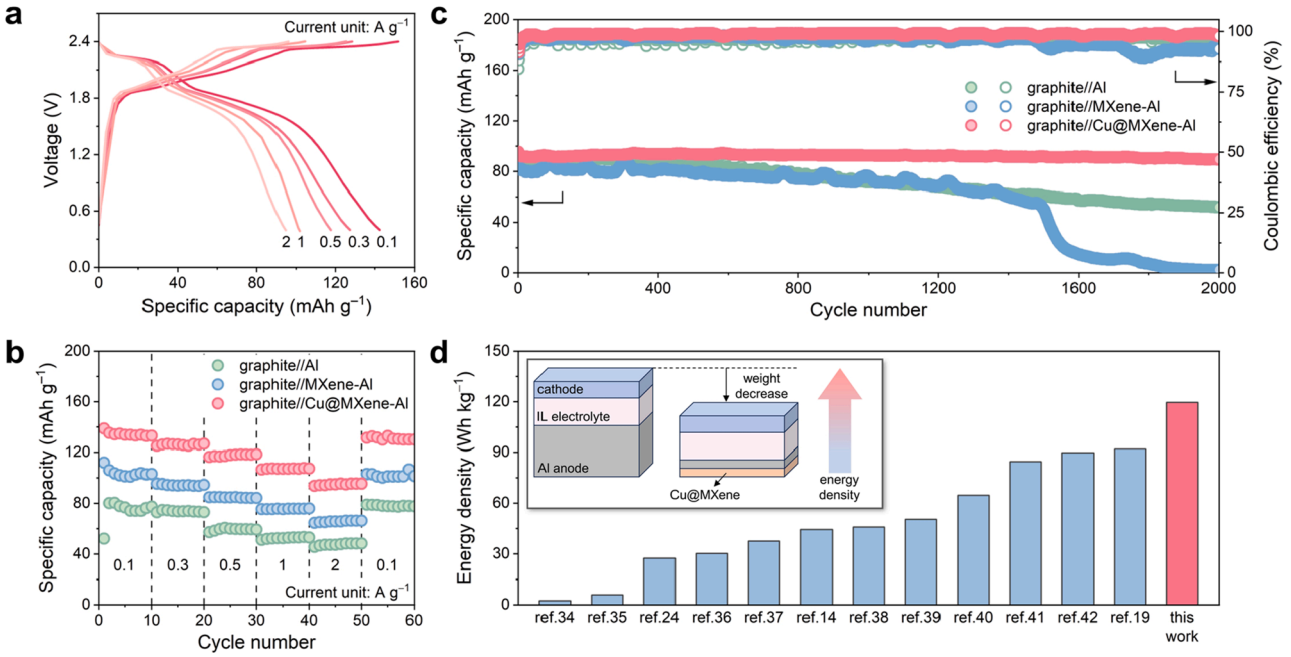

Fig. 5. Application of Cu@MXene-Al anode in AIB full cells. a) Galvanostatic charge/discharge profiles of graphite//Cu@MXene-Al full cells at various current densities. b) Rate performance of graphite//Al, graphite//MXene-Al and graphite//Cu@MXene-Al full cells at current densities from 0.1 A g^{-1} to 2 A g^{-1}. c) Cycling performance of graphite//Al, graphite//MXene-Al and graphite//Cu@MXene-Al full cells at 1 A g^{-1}. d) Comparison of energy densities of AIBs based on carbonaceous cathode between this work and existing studies. Inset is the schematic illustration showing the design of high-energy-density AIBs achieved through reducing N/P ratio.

curation. **Xiaoyue Zhang:** Investigation, Formal analysis, Data curation. **Chaoqun Li:** Investigation, Formal analysis. **Yingxue Li:** Investigation. **Panyu Gao:** Investigation. **Sihan Yin:** Investigation. **Tengfei Zhang:** Investigation, Formal analysis. **Guanglin Xia:** Supervision, Formal analysis. **Baozhong Liu:** Writing – review & editing, Supervision, Funding acquisition. **Xuebin Yu:** Writing – review & editing, Supervision, Project administration, Funding acquisition.

Declaration of competing interest

The authors declare that they have no known competing financial interests or personal relationships that could have appeared to influence the work reported in this paper.

Acknowledgments

This work was partially supported by the National Natural Science Foundation of China (U22A20120) and the China Postdoctoral Science Foundation (2023M740639).

Supplementary materials

Supplementary material associated with this article can be found, in the online version, at doi:10.1016/j.ensm.2025.104232.

Data availability

Data will be made available on request.

References

[1] M. Li, J. Lu, X. Ji, Y. Li, Y. Shao, Z. Chen, C. Zhong, K. Amine, Design strategies for nonaqueous multivalent-ion and monovalent-ion battery anodes, Nat. Rev. Mater. 5 (2020) 276–294.
[2] H. Yang, H. Li, J. Li, Z. Sun, K. He, H.M. Cheng, F. Li, The rechargeable aluminum battery: opportunities and challenges, Angew. Chem. Int. Ed. 58 (2019) 11978–11996.
[3] J. Meng, X. Yao, X. Hong, L. Zhu, Z. Xiao, Y. Jia, F. Liu, H. Song, Y. Zhao, Q. Pang, A solution-to-solid conversion chemistry enables ultrafast-charging and long-lived molten salt aluminium batteries, Nat. Commun. 14 (2023) 3909.
[4] J. Tu, W.L. Song, H. Lei, Z. Yu, L.L. Chen, M. Wang, S. Jiao, Nonaqueous rechargeable aluminum batteries: progresses, challenges, and perspectives, Chem. Rev. 121 (2021) 4903–4961.
[5] F. Wu, H. Yang, Y. Bai, C. Wu, Paving the path toward reliable cathode materials for aluminum-ion batteries, Adv. Mater. 31 (2019) 1806510.
[6] X. Han, Y. Bai, R. Zhao, Y. Li, F. Wu, C. Wu, Electrolytes for rechargeable aluminum batteries, Prog. Mater. Sci. 128 (2022) 100960.
[7] M. Jiang, C. Fu, P. Meng, J. Ren, J. Wang, J. Bu, A. Dong, J. Zhang, W. Xiao, B. Sun, Challenges and strategies of low-cost aluminum anodes for high-performance Al-based batteries, Adv. Mater. 34 (2021) 2102026.
[8] B. Long, F. Wu, Y. Li, H. Yang, W. Liu, Y. Li, Q. Li, X. Feng, Y. Bai, C. Wu, Manipulating the corrosion homogeneity of aluminum anode toward long-life rechargeable aluminum battery, Carbon Neutralization 3 (2023) 64–73.
[9] J. Tu, C. Chang, M. Wang, W. Guan, S. Jiao, Stable and low-voltage-hysteresis zinc negative electrode promoting aluminum dual-ion batteries, Chem. Eng. J. 430 (2022) 132743.
[10] H. Chen, H. Xu, B. Zheng, S. Wang, T. Huang, F. Guo, W. Gao, C. Gao, Oxide film efficiently suppresses dendrite growth in aluminum-ion battery, ACS. Appl. Mater. Interfaces 9 (2017) 22628–22634.
[11] N. Li, D. She, K. Zhang, H.S. Chen, W.L. Song, S. Jiao, Toward stable Al negative electrodes of aluminum-ion batteries: kinetic parameters and electrode structure, ChemSusChem 15 (2022) e202201390.
[12] Y. Long, H. Li, M. Ye, Z. Chen, Z. Wang, Y. Tao, Z. Weng, S. Qiao, Q. Yang, Suppressing Al dendrite growth towards a long-life Al-metal battery, Energy Storage Mater. 34 (2021) 194–202.
[13] J. Zheng, D.C. Bock, T. Tang, Q. Zhao, J. Yin, K.R. Tallman, G. Wheeler, X. Liu, Y. Deng, S. Jin, A.C. Marschilok, E.S. Takeuchi, K.J. Takeuchi, L.A. Archer, Regulating electrodeposition morphology in high-capacity aluminium and zinc battery anodes using interfacial metal–substrate bonding, Nat. Energy 6 (2021) 398–406.
[14] S. Wang, Y. Guo, X. Du, L. Xiong, Z. Liang, M. Ma, Y. Xie, W. You, Y. Meng, Y. Liu, M. Liu, Preferred crystal plane electrodeposition of aluminum anode with high lattice-matching for long-life aluminum batteries, Nat. Commun. 15 (2024) 6476.
[15] C. Yan, C. Lv, B.E. Jia, L. Zhong, X. Cao, X. Guo, H. Liu, W. Xu, D. Liu, L. Yang, J. Liu, H.H. Hng, W. Chen, L. Song, S. Li, Z. Liu, Q. Yan, G. Yu, Reversible Al metal anodes enabled by amorphization for aqueous aluminum batteries, J. Am. Chem. Soc. 144 (2022) 11444–11455.
[16] Y. Meng, J. Wang, M. Wang, Q. Peng, Z. Xie, Z. Zhu, Z. Liu, W. Wang, K. Zhang, H. Liu, Y. Ma, Z. Li, W. Chen, Anode-free aluminum electrode with ultralong cycle life and high coulombic efficiency exceeding 99.92 % enabled by a lattice-matching layer, Adv. Energy Mater. 13 (2023) 2301322.
[17] Q. Ran, H. Shi, H. Meng, S.P. Zeng, W.B. Wan, W. Zhang, Z. Wen, X.Y. Lang, Q. Jiang, Aluminum-copper alloy anode materials for high-energy aqueous aluminum batteries, Nat. Commun. 13 (2022) 576.
[18] T. Xu, L. Yao, G. Xia, X. Yu, Self-healing liquid metal layer as high-capacity and long cycle life anode for Al-ion batteries, Energy Storage Mater. 63 (2023) 103057.
[19] L. Wang, X. Song, Y. Hu, W. Yan, Z. Tie, Z. Jin, Initial-anode-free aluminum ion batteries: in-depth monitoring and mechanism studies, Energy Storage Mater. 44 (2022) 461–468.
[20] Y. Meng, M. Wang, K. Li, Z. Zhu, Z. Liu, T. Jiang, X. Zheng, K. Zhang, W. Wang, Q. Peng, Z. Xie, Y. Wang, W. Chen, Reversible, dendrite-free, high-capacity aluminum metal anode enabled by aluminophilic interface layer, Nano Lett. 23 (2023) 2295–2303.
[21] S. Wang, Y. Guo, X. Du, L. Xiong, Z. Huang, X. Li, Y. Xie, M. Ma, Z. Liang, Bottom growth strategy for high areal capacity rechargeable aluminum batteries, Nano Energy 114 (2023) 108626.
[22] S. Wang, Y. Guo, X. Du, L. Xiong, Z. Huang, X. Li, M. Ma, Z. Liang, Y. Xie, Space limited growth strategy for ultra-high areal capacity rechargeable aluminum batteries, Energy Storage Mater. 60 (2023) 102826.
[23] H. Yang, L. Yin, J. Liang, Z. Sun, Y. Wang, H. Li, K. He, L. Ma, Z. Peng, S. Qiu, C. Sun, H.M. Cheng, F. Li, An aluminum–sulfur battery with a fast kinetic response, Angew. Chem. Int. Ed. 57 (2018) 1898–1902.
[24] S. Ju, Q. Qiao, T. Xu, Z. Zhao, T. Zhang, G. Xia, X. Yu, Stable aluminum metal anode enabled by dual-functional molybdenum nanoparticles, Small 20 (2024) 2308632.
[25] L. Yao, S. Ju, T. Xu, W. Wang, X. Yu, MXene-based mixed conductor interphase for dendrite-free flexible Al organic battery, ACS Nano 17 (2023) 25027–25036.
[26] Y. Yang, X. Li, G. Liu, H. Liu, Y. Shi, C. Ye, Z. Fang, M. Ye, J. Shen, Hierarchical ohmic Contact interface engineering for efficient hydrazine-assisted hydrogen evolution reaction, Adv. Mater. 36 (2024) 2307979.
[27] Z. Chen, T. Ma, W. Wei, W.Y. Wong, C. Zhao, B.J. Ni, Work function-guided electrocatalyst design, Adv. Mater. 36 (2024) 2401568.
[28] Y.S. Feng, Y.N. Li, P. Wang, Z.P. Guo, F.F. Cao, H. Ye, Work-function-induced interfacial electron/ion transport in carbon hosts toward dendrite-free lithium metal anodes, Angew. Chem. Int. Ed. 62 (2023) e202310132.
[29] Y. Deng, T. Shang, Z. Wu, Y. Tao, C. Luo, J. Liang, D. Han, R. Lyu, C. Qi, W. Lv, F. Kang, Q.H. Yang, Fast gelation of $Ti_3C_2T_x$ MXene initiated by metal ions, Adv. Mater. 31 (2019) 1902432.
[30] S. Guan, Z. Yuan, Z. Zhuang, H. Zhang, H. Wen, Y. Fan, B. Li, D. Wang, B. Liu, Why do single-atom alloys catalysts outperform both single-atom catalysts and nanocatalysts on MXene? Angew. Chem. Int. Ed. 63 (2023) e202316550.
[31] X. Zhang, Y. Sun, S. Ju, J. Ye, X. Hu, W. Chen, L. Yao, G. Xia, F. Fang, D. Sun, X. Yu, Solar-driven reversible hydrogen storage, Adv. Mater. 35 (2023) 2206946.
[32] G. Deysher, J.A.S. Oh, Y.-T. Chen, B. Sayahpour, S.-Y. Ham, D. Cheng, P. Ridley, A. Cronk, S.W.-H. Lin, K. Qian, L.H.B. Nguyen, J. Jang, Y.S. Meng, Design principles for enabling an anode-free sodium all-solid-state battery, Nat. Energy 9 (2024) 1161–1172.
[33] C. Wang, C. Yang, Y. Du, Z. Guo, H. Ye, Spherical lithium deposition enables high Li-utilization rate, low negative/positive ratio, and high energy density in lithium metal batteries, Adv. Funct. Mater. 33 (2023) 2303427.
[34] X.Z. Yu, B. Wang, D.C. Gong, Z. Xu, B.G. Lu, Graphene nanoribbons on highly porous 3D Graphene for high-capacity and ultrastable Al-ion batteries, Adv. Mater. 29 (2017) 1604118.
[35] M.C. Lin, M. Gong, B. Lu, Y. Wu, D.Y. Wang, M. Guan, M. Angell, C. Chen, J. Yang, B.J. Hwang, H. Dai, An ultrafast rechargeable aluminium-ion battery, Nature 520 (2015) 324–328.
[36] Z. Liu, J. Wang, X. Jia, W. Li, Q. Zhang, L. Fan, H. Ding, H. Yang, X. Yu, X. Li, B. Lu, Graphene armored with a crystal carbon shell for ultrahigh-performance potassium ion batteries and aluminum batteries, ACS Nano 13 (2019) 10631–10642.
[37] H. Chen, H. Xu, S. Wang, T. Huang, J. Xi, S. Cai, F. Guo, Z. Xu, W. Gao, C. Gao, Ultrafast all-climate aluminum-graphene battery with quarter-million cycle life, Sci. Adv. 3 (2017) eaao7233.
[38] D.Y. Wang, C.Y. Wei, M.C. Lin, C.J. Pan, H.L. Chou, H.A. Chen, M. Gong, Y. Wu, C. Yuan, M. Angell, Y.J. Hsieh, Y.H. Chen, C.Y. Wen, C.W. Chen, B.J. Hwang, C. C. Chen, H. Dai, Advanced rechargeable aluminium ion battery with a high-quality natural graphite cathode, Nat. Commun. 8 (2017) 14283.
[39] J. Li, K.S. Hui, S. Ji, C. Zha, C. Yuan, S. Wu, F. Bin, X. Fan, F. Chen, Z. Shao, K. N. Hui, Electrodeposition of a dendrite-free 3D Al anode for improving cycling of an aluminum-graphite battery, Carbon Energy 4 (2022) 155–169.
[40] C. Li, P.C. Rath, S.-X. Lu, J. Patra, C. Su, D. Bresser, S. Passerini, J. Chang, Ordered nano-structured mesoporous CMK-8 and other carbonaceous positive electrodes for rechargeable aluminum batteries, Chem. Eng. J. 417 (2021) 129131.
[41] Y.H. Heo, J. Lee, S. Ha, J. Chan Hyun, D.H. Kang, J. Yoon, H.S. Kim, Y. Choi, Y. Chan Kang, H.-J. Jin, S.J. Kim, Y.S. Yun, 3D-structured bifunctional MXene paper electrodes for protection and activation of Al metal anodes, J. Mater. Chem. A 11 (2023) 14380–14389.
[42] Y. Kong, C. Tang, X. Huang, A.K. Nanjundan, J. Zou, A. Du, C. Yu, Thermal reductive perforation of graphene cathode for high-performance aluminum-ion batteries, Adv. Funct. Mater. 31 (2021) 2010569.